J Mater Sci: Mater Electron (2023) 34:955

Optical response of Eu^{3+}-activated $MgAl_2O_4$ nanophosphors for Red emissive

LED Applications

B. Nageswara Rao[1,2,3], P. Tirupathi Rao[1], Sk. Esub Basha[1], D. S. L. Prasanna[4,6], K. Samatha[2], and R. K. Ramachandra[1,5,*]

[1] *Crystal Growth and Nano-Science Research Center, Department of Physics, Government College (A), Rajamahendravaram 533105, Andhra Pradesh, India*
[2] *Department of Physics, Andhra University, Visakhapatnam 530003, Andhra Pradesh, India*
[3] *Department of Physics, Dr V S Krishna Government Degree College (A), Visakhapatnam, India*
[4] *Department of Chemistry, Acharya Nagarjuna University, Guntur 522510, A.P, India*
[5] *Government Degree College, Chodavaram, Visakhapatnam 531036, Andhra Pradesh, India*
[6] *Department of Chemistry, Dr V S Krishna Government Degree College (A), Visakhapatnam, India*

Received: 28 December 2022
Accepted: 25 March 2023

ABSTRACT

Eu^{3+}-activated magnesium aluminate phosphors were successfully synthesized by nitrate–citrate gel combustion method and thermally treated at 650, 750, 850, and 950°C. The powder X-ray diffraction pattern showed that all $MgAl_2O_4$:-$x Eu^{3+}$ ($0 \leq x \leq 0.10$) samples exhibit crystallized cubic phase of spinel structure with space group Fd-3 m. The Debye–Scherrer equation is used to estimate average crystallite size values and are found to be 8.5–12.1 nm, that are also confirmed by high-resolution transmission electron microscopy (HRTEM) images. TGA–DTG results suggest that the maximum decomposition of the precursors were observed below 600°C. Accordingly, the decomposition temperature was taken 650°C and above. The functional groups of the powder samples were determined by FTIR. Energy levels were characterized, and the band gap energy (E_g) has been calculated using UV–Vis absorption spectroscopy and found to be in the range of 5.08–5.19 eV. The FESEM images shows that the nanoparticles are agglomerated and are in nonuniform spherical shape with reduced average particle size from 27 ± 4.1 to 24.1 ± 3.3 nm. Further, the elemental composition of the as-prepared samples was analyzed by using energy-dispersive X-ray spectra (EDAX). The photoluminescent property of $MgAl_2O_4$:xEu^{3+} samples was investigated using room-temperature emission spectroscopy. These phosphors show different emissions of Eu^{3+} corresponding to $^5D_0 \rightarrow {}^7F_{J=1,2,3,4}$ transitions which lie in the wavelength range from 590 to

Address correspondence to E-mail: drkrcr@gmail.com; ramc@gcrjy.ac.in

https://doi.org/10.1007/s10854-023-10341-w
Published online: 13 April 2023

703 nm. The red emission transition $^5D_0 \rightarrow {}^7F_2$ ($\Delta J = 2$) centered at 612 nm has been known to be hypersensitive, strong, and more intense of all samples. The PL emission intensity increases up to 4 mol% Eu^{3+} concentration and then decreases due to the process of concentration quenching. The chromaticity color coordinates were obtained from the luminescence emission spectrum. The temperature-dependent luminescence property of $MgAl_2O_4$:4%Eu^{3+} phosphor has also been discussed. These results showed that $MgAl_2O_4$:$x$$Eu^{3+}$ could be a prominent material for the production of artificial red light in red LEDs.

1 Introduction

Spinel oxides with the formula AB_2O_4, where A and B are divalent and trivalent cations, respectively, were effectively used as electric, magnetic, catalysis, ceramic, chemical, electronic, and optical materials [1]. They have also been acted as a stable host for persistent luminescence when rare-earth (RE)/transition-metal ions are incorporated into the host lattice [2].

Magnesium Aluminate spinel (MAS) with chemical formula $MgAl_2O_4$, where Mg^{2+} divalent metal cation normally occupies a tetrahedral site and Al^{3+} trivalent metal cations occupy the octahedral sites of a cubic packed crystal [3] have the cubic space group Fd-3 m. $MgAl_2O_4$ spinel is a ternary oxide with face center cubic structure (fcc) is one of the most important optically transparent materials that exhibit excellent properties such as high melting point, low thermal expansion coefficient, high mechanical strength, low density, high chemical resistance to both acidic and basic slags, relatively low dielectric loss, high thermal shock resistance, wide optical band gap, moderate refractive index, good poisson's ratio, excellent hot strength, high resistance to changes in the environment, resistance to slag corrosion, and excellent catalytic properties [4–8]. MAS has been widely employed in many industrial applications including color display, humidity sensors [9], tuneable solid-state lasers, refractory materials [10], lamp industry, catalyst supports [11], and transparent ceramics [12].

$MgAl_2O_4$ spinel doped with RE ions have been employed in luminescent and picture tube applications and this incorporation enhances the emission efficiency of the phosphor materials. $MgAl_2O_4$ has also been used as host material for glow phosphors doped with Mn^{2+} [13], Ti^{4+} [14], Nd^{3+} [15], Dy^{3+} [16], Mn^{2+}, Cr^{3+} [17], Er^{3+}, Yb^{3+} [18], Ti^{4+}, Mn^{2+} [19], Gd^{3+} [20], Eu^{2+} [21], Tb^{3+} [22], Eu^{3+}, Dy^{3+} [23], and Sm^{3+} [24]. Several preparative methods have been used for the synthesis of spinel nanophosphors including solid-state reaction method [25], co-precipitation, spray-drying, microwave-assisted hydrothermal method, sol-gel synthesis, molten salt process, nebulized spray pyrolysis (NSP) [26], solvothermal method, polyol method, aqueous wet chemical method, and combustion methods [20]. In the present investigation, we have reported the synthesis of Eu^{3+}-doped magnesium aluminate spinel's ($MgAl_2O_4$:$x$$Eu^{3+}$, $0 \leq x \leq 0.10$) by citrate–nitrate gel combustion method [18]. This preparation technique has been chosen because, it can produce a homogenous product in a short amount of time, offers low temperature initiation, excellent particle size distribution, less cost effective, high purity, and good morphological control. We have been investigated the influence of Eu^{3+} doping concentration on structural from powder X-ray diffraction (XRD), optical from UV–Vis, spectroscopic from FTIR, microstructural from FESEM, elemental composition from EDAX, morphological from HRTEM, and luminescent properties from emission spectra. The valence mismatch between Mg^{2+} and Eu^{3+} and their difference in size can be manifested by broad emission bands [15].

In this paper, we also demonstrated the $MgAl_2O_4$ spinel as an active host material for the luminescence as well as for the energy transfer to doped Eu^{3+} ions in the application of high efficiency phosphors for red LEDs. Eu^{3+}-activated $MgAl_2O_4$ is reported to be synthesized using a simple citrate–nitrate gel combustion method, which is considered as an active phosphor material for the development of pure red LEDs in optoelectronic applications. I. Omkaram et al. have already been investigated the photoluminescence study on $MgAl_2O_4$:Eu^{3+} phosphor in the literature [25] and the incorporated Eu^{3+} ion is

observed to emit red color in the emission spectrum. However, the study of the effect of high annealing temperature on the photoluminescence emission of $MgAl_2O_4$:4%Eu^{3+} has not been investigated in the literature to the best of our knowledge. The main objective of the present work is to study the optical properties of the as-synthesized pure and Eu^{3+}-doped $MgAl_2O_4$ samples as a function of Eu^{3+} doping concentration (2, 4, 6, 8, and 10 mol%) and their temperature-dependent photoluminescence investigations for optimal concentration (4 mol% Eu^{3+}) at progressively high annealing temperatures (650, 750, 850, and 950°C). The observed emission channels and CIE color coordinates of $MgAl_2O_4$:$x$$Eu^{3+}$ phosphor materials were also reported in detail.

2 Experimental section

2.1 Sample synthesis

Figure 1 shows the synthesis of Eu^{3+}-doped $MgAl_2O_4$ powders. All analytical grade reagent chemicals were purchased and used without further purification in this experimental study. The precursors used for the synthesis are listed in Table 1. Citrate–nitrate gel combustion process was employed to prepare the bare and Eu^{3+}-doped $MgAl_2O_4$ nanophosphors using magnesium nitrate hexahydrate [$Mg(NO_3)_2{\cdot}6H_2O$], aluminum nitrate nonahydrate [$Al(NO_3)_3{\cdot}9H_2O$], and Citric Acid [$C_6H_8O_7.H_2O$] as starting materials. Metal nitrates were added as oxidizers and citric acid was used as a chelating agent. Each material was weighed by using a high precision (0.0001 g) balance. The procedure used to prepare Eu^{3+}-doped $MgAl_2O_4$ nanophosphors as follows: Stoichiometric amounts of $Al(NO_3)_3{\cdot}9H_2O$ and $Mg(NO_3)_2{\cdot}6H_2O$ and Citric Acid ($C_6H_8O_7.H_2O$) were dissolved in deionized water (D. W.) and subsequent sonication as well as mixing at ambient temperature for 1 h to obtain transparent solution. In addition, Eu_2O_3 is dissolved in dilute HNO_3 to prepare homogeneous solution, which is slowly added to the above resultant solution. Subsequently, the final precursor solution was placed into glass containers and introduced onto a Magnetic stirrer at 120 °C until the formation of a brown resin as a burnt ash product. After that the above product was transferred into a silica crucible and calcined in a muffle furnace at 650, 750, 850, and 950°C for 12 h in air atmosphere to obtain Eu^{3+}-doped $MgAl_2O_4$ phosphors. The mole concentration of the activator Eu^{3+} ion varied as 0.02, 0.04, 0.06, 0.08, and 0.10 from an appropriate stoichiometric ratio.

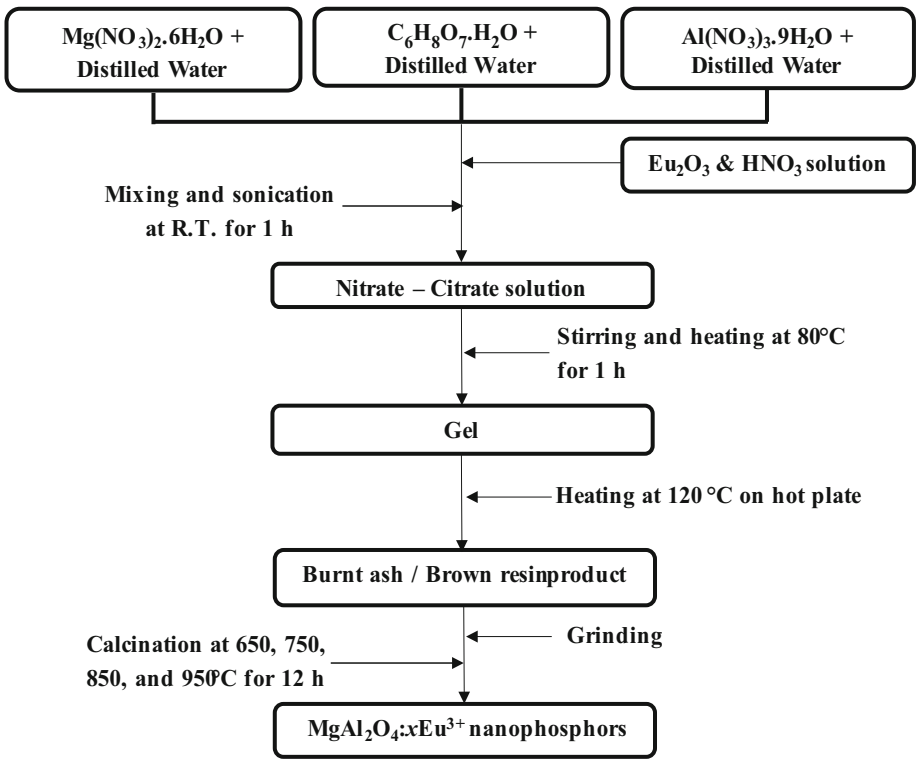

Fig. 1 Flowchart of the synthesis procedure of $MgAl_2O_4$:$x$$Eu^{3+}$ nanophosphors by nitrate–citrate gel combustion method

Table 1 Primary chemicals used for synthesis of Eu^{3+}-doped $MgAl_2O_4$ powders

Chemical name	Chemical formula	Molecular Weight (g/mol)	Purity	Manufacturer
Magnesium nitrate hexahydrate	$Mg(NO_3)_2{\cdot}6H_2O$	256.41	99.0%	Fisher Scientific
Aluminum nitrate nonahydrate	$Al(NO_3)_3{\cdot}9H_2O$	375.13	98.0%	Fisher Scientific
Citric Acid	$C_6H_8O_7$	192.12	99.5%	Fisher Scientific
Europium(III) oxide	Eu_2O_3	351.93	99.9%	Sigma-Aldrich

2.2 Sample characterization

The phase purity and crystallinity of Eu^{3+}-doped $MgAl_2O_4$ phosphors were examined by powder X-ray diffraction measurements using PANalytical X′pert Pro diffractometer, CuKα radiation (K = 1.5406 Å) with a nickel filter. For XRD analysis, data were collected at a scan rate of 1°/min with a 0.02° step size for 2θ from 10° to 80°. Thermal gravimetric analysis of the precursors was performed using TG–DTA analyzer (NETZSCH STA 409) in the range temperature 35–950°C with SiC as heating element. FTIR spectra were recorded using PerkinElmer Spectrometer, Frontier using KBr as a reference after calcinations in the wavenumber range 4000–400 cm^{-1}. UV–visible diffuse reflectance spectra (DRS) were performed in an Agilent Cary 5000 UV–Vis NIR spectrometer with an attached diffuse reflectance accessory in the wavelength range of 200–800 nm to estimate the energy band gap of the samples. Field emission scanning electron microscope (FESEM, Hitachi S-4800) was used to examine surface morphology of the prepared nanophosphors. High-resolution transmission electron microscopy (HRTEM) images were made using JEOL JEM 2100 to investigate the crystalline structure of the samples. The Photoluminescence (PL) studies have been carried out using a Horiba Flurolog-3 spectrofluorometer (450 W Xenon lamp). All the measurements were performed at room temperature. The chromaticity color coordinates of the samples were recorded according to the Commission Internationale de l'Eclairage (CIE) by using Spectra Lux Software v.2.0 Beta.

3 Results and discussion

3.1 Powder X-Ray diffraction (XRD) studies

The phase purity and crystal structure of the undoped and Eu^{3+}-doped $MgAl_2O_4$ nanophosphors prepared by nitrate–citrate gel combustion were analyzed using the powder X-ray diffraction data. The PXRD patterns of the $MgAl_2O_4$:xEu^{3+} ($0 \leq x \leq 0.10$) powders are shown in Fig. 2a. All the observed diffraction peaks of the samples have been indexed to the pure cubic phase of $MgAl_2O_4$ of space group: O^7_h (*Fd*-3 *m*) with the spinel-type structure which is well comparable with the standard pattern [JCPDS # 21-1152] [23]. No additional peaks were detected for the doped $MgAl_2O_4$ up to 10 mol% of Eu^{3+} doping level indicates that the Eu elements are homogeneously mixed and may be well doped into the $MgAl_2O_4$ lattice. The higher intensities of peaks of annealed samples with narrower width suggest a complete formation of highly crystallized the spinel structure. The average crystallite size of the Eu^{3+}-doped $MgAl_2O_4$ nanoparticles was calculated using the Scherrer formula:

$$D = \frac{K\lambda}{\beta(2\theta)\cos\theta}, \quad (1)$$

where λ is the wavelength of the incident X-rays (1.5406Å), θ is the diffraction angle, β(2θ) being the full width at half maximum (FWHM) of the observed diffraction peak in radians, K is 0.9, and D is the average diameter of the crystallite, respectively [22]. The prepared samples show several diffraction peaks have been indexed to (111), (220), (311), (400), (422), (511), (440), (531), (620), and (533) miller planes of high and moderate intensities as shown in Fig. 2a. The average crystalline size (D) of $MgAl_2O_4$:$x$$Eu^{3+}$ was estimated from the X-ray line broadening and is reduced from 12.1 to 8.5 nm by the incorporation of

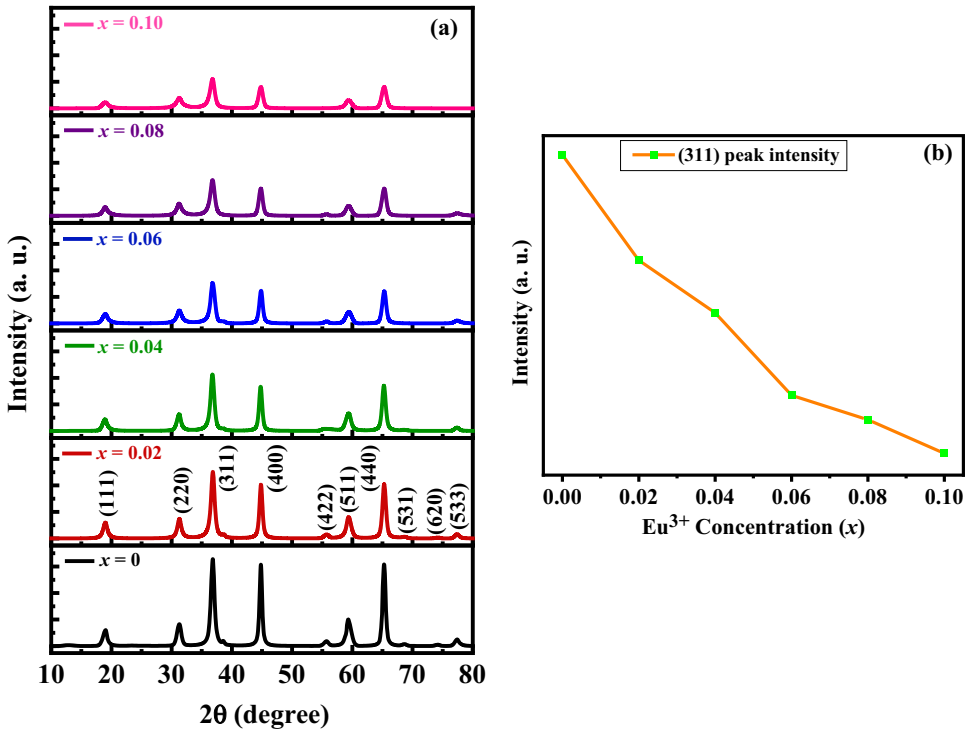

Fig. 2 **a** The powder XRD pattern of $MgAl_2O_4$:xEu^{3+} ($0 \le x \le 0.10$) series calcined at 950 °C for 12 h. **b** Variation of (311) peak intensity in the powder XRD pattern with Eu substitution

Eu^{3+} from 0.0 to 0.10 revealing the presence of nanosized particles in the grown phosphors. Figure 2b shows that the XRD peak intensities were slightly decreased with an increase of Eu^{3+} doping content, which indicates reduced crystallinity [27]. The reduced crystallinity is consistent with the decreased crystalline sizes of $MgAl_2O_4$:xEu^{3+} phosphors evaluated from the peak widths using Debye–Scherrer equation.

Figure 3 shows the variation of the microstructural parameters, the lattice constant (a), the crystallite size (D), dislocation density (δ), and microstrain (ε) with Eu^{3+} concentration. The overall increase in the dislocation density and microstrain with increasing Eu^{3+} content is attributed to either (i) due to the creation of some stresses and strains caused by the incorporation of Eu element into the $MgAl_2O_4$ crystal lattice or (ii) due to increased grain boundaries (Fig. 3b) [13]. Figure 3a shows the variation of the lattice parameter and the crystallite size (D) with the addition of Eu^{3+}. The lattice constant and crystallite size that relatively decreased with increasing Eu^{3+} doping concentration may be attributed to the lattice distortion caused by the difference in ionic radius between Eu^{3+} (1.07 Å) and Mg^{2+} (0.78Å) and it indicates that Eu^{3+} is successfully incorporated into host lattice and occupy Mg^{2+} tetrahedral sites. Figure 3d demonstrates the variation of unit cell volume of $MgAl_2O_4$:xEu^{3+} as a function of Eu^{3+} content.

The cation–anion bond lengths at octahedral and tetrahedral sites are denoted with d_{Al-O} and d_{Mg-O}, respectively. The bond distances of Mg–O and Al–O are defined as [28]

$$d_{Mg-o} = \sqrt{3}a(u - 1/4) \tag{2}$$

$$d_{Al-O} = a\sqrt{(u - 5/8)^2 + 2(u - 3/5)^2}, \tag{3}$$

where a is the lattice parameter and u is the positional parameter of the oxygen atoms referred to the origin at -43 m in the space group of Fd-3 m. The bond lengths of Mg–O and Al–O decrease with increasing the Eu^{3+} doping concentration in an approximated linear fashion (Fig. 3c). The two bond lengths cross each other, with Al–O larger than Mg–O at concentrations lower than 6 mol% Eu^{3+} and vice versa [29, 30]. Close to this concentration, Al–O and Mg–O bond lengths become equal in the spinel structure.

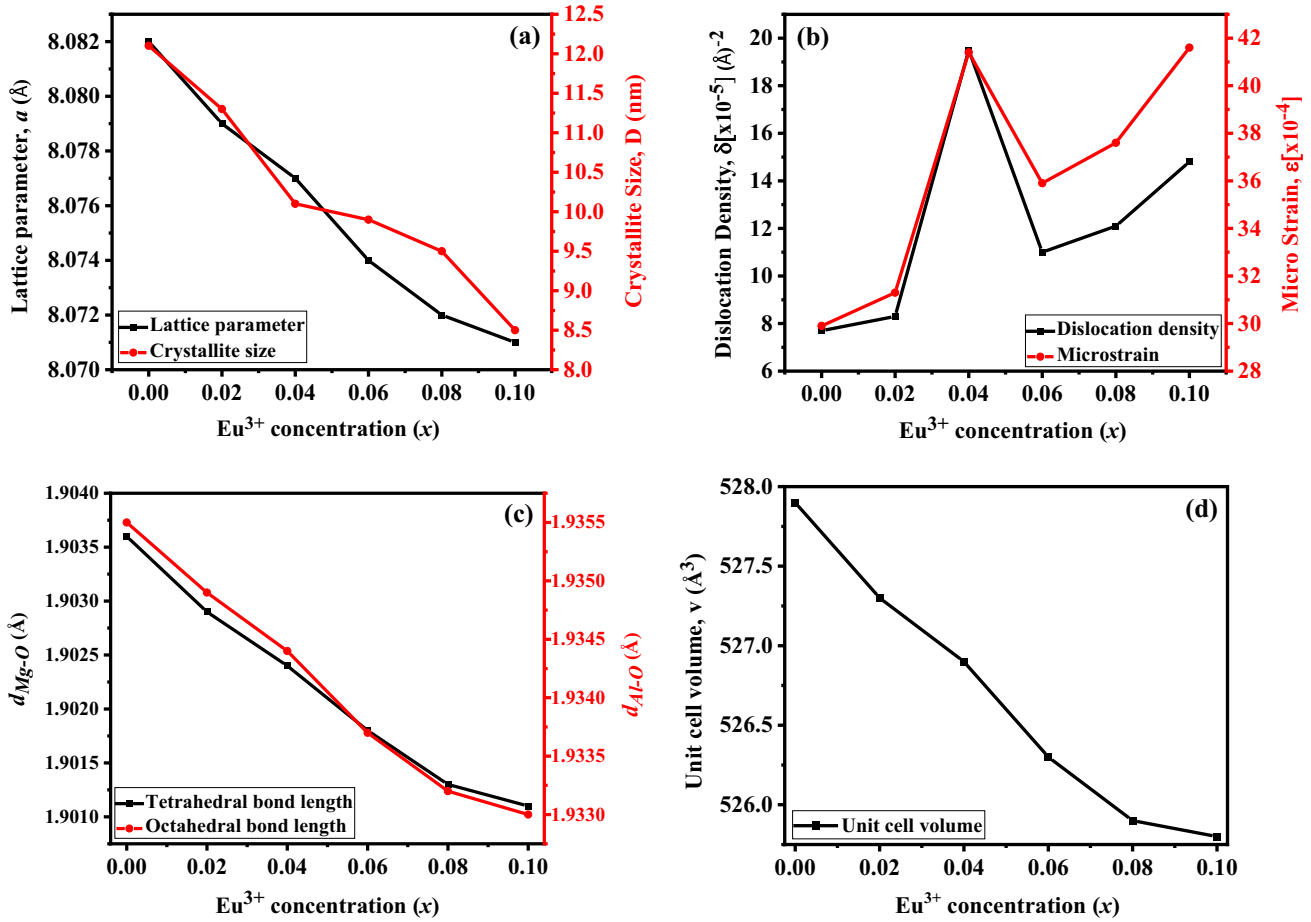

Fig. 3 Structural parameters variation of $MgAl_2O_4$:xEu^{3+} with Eu^{3+} doping concentration **a** Lattice parameter and Average crystallite size; **b** Dislocation density and Microstrain; **c** Bond lengths of Mg–O and Al–O; and **d** Avg. unit cell volume

3.2 Thermogravimetric analysis (TGA)

Decomposition of basic combustion-gel product was analyzed by plotting percentage weight against temperature (TGA curve), while the origins of exothermic/endothermic peaks were studied by DTA [31]. The stability/decomposition of $MgAl_2O_4$:10 mol% Eu^{3+} precursor compound have been done on Thermogravimetric analysis upto 950 °C in the presence of N_2 gas (Fig. 4). In the initial stage, the weight loss of 8.06 wt% below the temperature of 170 °C (peak at 102 °C) is due to the evaporation of physically adsorbed water. The second weight loss of 17.04 wt% occurs in the range of 180–325 °C with peak at 265 °C, due to the release of nitrogen and oxygen. Further, in the third stage, the weight loss of 20.45 wt% observed in the temperature range of 330-440°C (peak at 390 °C) can be attributed to the removal of CO_2 and residual organic moieties. A small peak at 480°C with a slight weight loss likely

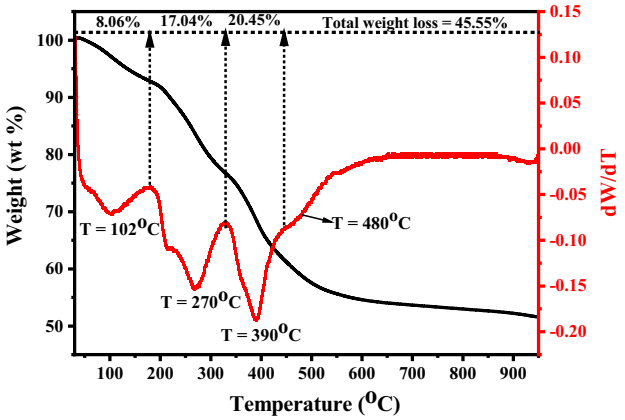

Fig. 4 TGA and DTG curves of dried citrate–nitrate gel product of $MgAl_2O_4$:xEu^{3+} (x = 0.10)

belongs to the incomplete crystallization [32]. From TGA–DTG results, no apparent weight loss occurs above 550–600°C. This indicates and confirms that the stable $MgAl_2O_4$ spinel phase is formed above 600 °C

[33, 34]. Hence, the calcination temperature of the as-prepared sample was taken as 600ºC or above.

3.3 Fourier transform infrared (FTIR) spectroscopic studies

Figure 5 shows the FTIR spectra recorded in the range 4000–500 cm^{-1} of $MgAl_2O_4$:xEu^{3+} powders. A strong broad band centered about 3465 cm^{-1} is associated with O–H stretching vibrations (symmetric & anti-symmetric) of molecular water adsorbed in the structure [24]. The characteristic band centered at 2345 cm^{-1} is corresponding to the atmospheric carbon dioxide (CO_2) absorption on metallic cations [35]. The peaks between 750 and 1200 cm^{-1} are due to O–H bending mode. Vibration bands present around 690 and 514 cm^{-1} are related to the inorganic network and their characteristic band peaks become much sharper with increasing doping concentration of Eu^{3+}. These peaks are attributed to the presence of AlO_6 groups and lattice vibration of Mg–O stretching. AlO_6 groups building up the $MgAl_2O_4$ phosphors, which is the only crystalline phase present as it was anticipated from the XRD studies of the calcined powders [16]. The vibration band at 1553 cm^{-1} can be assigned to H–O–H deformation bending mode. The absorption peak at 1382 cm^{-1} may be derived from the existence of nitrate [36]. The absorption peaks at 1170–980 cm^{-1} in the pure sample are assigned to the vibration of hydroxyl-metal (Mg or Al) bands [37, 38].

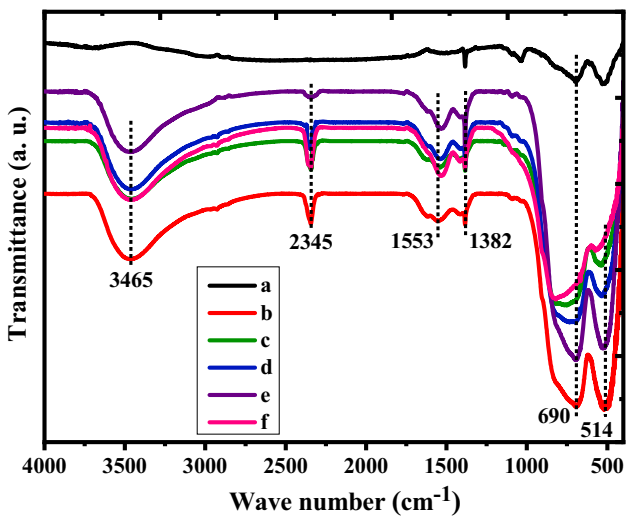

Fig. 5 Fourier transform infrared (FTIR) spectra of $MgAl_2O_4$:xEu^{3+} phosphors at 950ºC for 12 h [(**a**) $x = 0.00$, (**b**) $x = 0.02$, (**c**) $x = 0.04$, (**d**) $x = 0.06$, (**e**) $x = 0.08$, and (**f**) $x = 0.10$]

The shape of the absorption bands does not change and their areas and intensities are reduced in Eu^{3+}-doped samples. FTIR spectra confirmed the formation of pure $MgAl_2O_4$ with no other secondary phase or additional impurities. The broad to weak band around 690 cm^{-1} is related to the vibration frequency of Al^{3+} in octahedral site of AlO_6^{3-} groups due to the microstructure changes by the substitution of Eu^{3+} into host lattice (Table 2).

3.4 UV–visible diffuse reflectance spectroscopy

The absorption characteristics of undoped and Eu^{3+}-doped $MgAl_2O_4$ phosphors have been studied using the UV–Vis absorption spectroscopy. Figure 6(a) represents the absorption spectra of $MgAl_2O_4$:xEu^{3+} ($0 \le x \le 0.10$) samples, which shows three absorption bands situated around 215, 250, and 370 nm. The absorption peak centered at 215 nm may be assigned to emerge from band-to-band absorption of the unsubstituted material [13]. The strong absorption bands located at 250 nm can be associated to originate from $O^{2-}(2p) \rightarrow Al^{3+}(3d)$ charge transfer due to the electron's excitations from the valence band to conduction band in the host crystal lattice. The absorption band around 370 nm in the doped samples is arising from the characteristic transition of Eu^{3+} ions [39, 40]. It can be clearly observed that the intensity of absorption peak at 250 nm is increased with increasing Eu^{3+} content. This is attributed to the fact that the Eu^{3+} changing the occupational site by replacing the Mg^{2+} instead of Al^{3+} in the host material [27]. Moreover, the peak centered at 250 nm is blue shifted in the absorption spectra with increasing Eu^{3+} doping concentration in Eu^{3+}-activated $MgAl_2O_4$ phosphors, which indicates the enhanced band gap (E_g) values of Eu^{3+}-doped $MgAl_2O_4$. The UV–Vis absorption studies indicate and suggest that the variation in Eu^{3+} doping content controls the Eu^{3+} occupational site (Mg^{2+} and Al^{3+}) in the host lattice and it also affects the absorption.

The band gap energies of pure and Eu^{3+}-doped $MgAl_2O_4$ nanoparticles were evaluated by well-known Tauc's relation:

$$\alpha h\nu = A\left(h\nu - E_g\right)^n, \quad (4)$$

where h is the Planck's constant, A is a constant, E_g is the band gap energy (in eV), α is the absorption

Table 2 FTIR peaks and their assignments of the Eu^{3+}-doped $MgAl_2O_4$.

Eu^{3+} Conc. (x)	Peak position of the assignment (cm^{-1})				
	AlO_6 group	Vibration mode of nitrate	H–O–H bending vibration	Absorption of atmospheric CO_2 on metallic cations	O–H stretching
0.00	513 693	1384	1524	–	3665
0.02	511 690	1385	1555	2343	3463
0.04	532 750	1385	1541	2345	3465
0.06	534 732	1385	1538	2347	3466
0.08	528 702	1384	1532	2346	3469
0.10	568 812	1384	1528	2351	3468

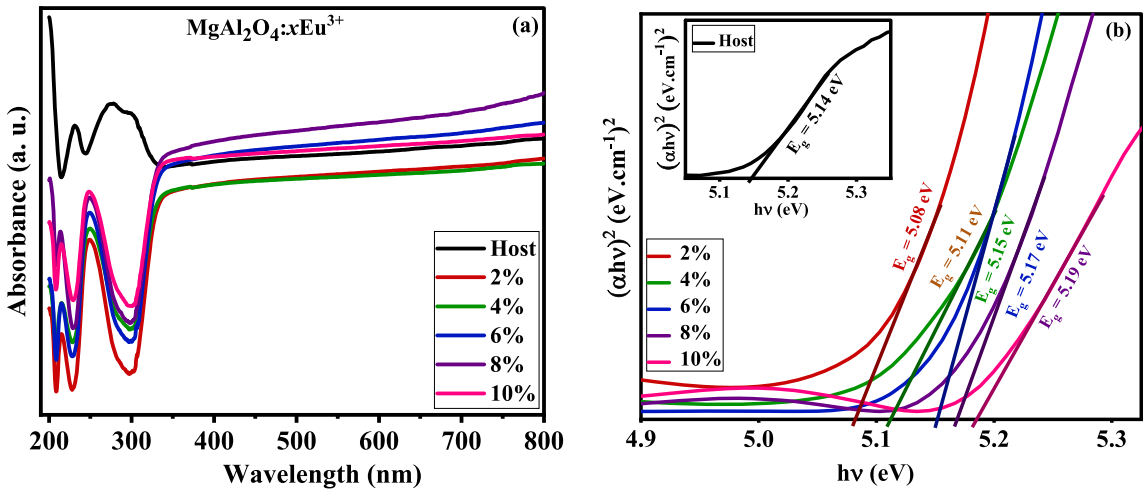

Fig. 6 **a** UV–Visible absorption spectra of $MgAl_2O_4$:xEu^{3+} phosphors at 950°C for 12 h; and **b** Tauc's plots of $(\alpha h\nu)^2$ vs. hν of $MgAl_2O_4$:xEu^{3+} phosphors with increase in Eu^{3+} concentrations (The inset shows Tauc's plot of Host material)

coefficient, ν is the incident photons frequency, and n equals to ½ for direct allowed transitions. The direct band gap E_g was estimated by extrapolating the linear fitted region to $[\alpha h\nu]^2 = 0$ in the tauc plot of $[\alpha h\nu]^2$ versus hν for absorption measurements, for $MgAl_2O_4$ as it is a direct band gap material. The band gap energy estimated from tauc's plot is 5.14 eV for pure $MgAl_2O_4$ and for Eu^{3+}-doped $MgAl_2O_4$, the E_g is increasing from 5.08 to 5.19 eV as shown in Fig. 6b [41, 42]. So, a quantum size effect is correlated for Eu^{3+}-doped $MgAl_2O_4$, where the band gap increases and crystallite size decreases with Eu^{3+} doping concentration. The absorption measurements suggest that varying the Eu^{3+} doping concentration regulates the band gap energy (Table 3).

Table 3 The band gap energy values of $MgAl_2O_4$:xEu^{3+} nanophosphors calculated by Tauc's plot

S. No.	Concentration of Eu^{3+}	Direct band gap energy E_g (eV)	Average crystallite size (nm)
1	0.0	5.14	12.1
2	0.02	5.08	11.3
3	0.04	5.11	10.1
4	0.06	5.15	9.9
5	0.08	5.17	9.5
6	0.10	5.19	8.5

3.5 FESEM analysis

The structure and the particle morphology of the synthesized nanopowders have been analyzed by Field emission scanning electron microscopy (FESEM) images. The magnified FESEM micrographs

of the pure, 2%, 6%, and 10% Eu^{3+}-substituted $MgAl_2O_4$ spinel phosphor nanoparticles are shown in Fig. 7(a–d). These images clearly show that most of the nanoparticles exhibited spherical shape with variable particle sizes. The average particle diameter of the as-prepared materials is expressed in mean size ± SD nm. The average sizes of pure, 2%, 6%, and 10% Eu^{3+}-doped $MgAl_2O_4$ NPs were estimated as 27 ± 4.1 nm, 25.9 ± 5.3 nm, 25 ± 3.8 nm, and 24.1 ± 3.3 nm, respectively (Fig. 8(a–d)). So, the estimated average particle size of the spherical like shaped particles decreases with increasing Eu^{3+} doping concentration [43]. It is also evidenced from the FESEM images that the incorporation of Eu^{3+} cations in $MgAl_2O_4$ lattice did not alter the particle morphology of the phosphor particles significantly. FESEM micrographs at higher magnification illustrate that the grains of the prepared samples are agglomerated with several nanoparticles, shown in Fig. 7(a–d). Further it has been observed that the as-synthesized samples demonstrate the porous nature, which is attributed to the evolution of various gases during the process of gel combustion at high temperatures [44, 45].

3.6 EDAX spectroscopy

The energy-dispersive X-ray spectroscopy (EDAX) and associated element ratios for pure and 10% Eu^{3+}-doped $MgAl_2O_4$ powders are presented in Fig. 9(a–b). Pure $MgAl_2O_4$ and $MgAl_2O_4$:10% Eu^{3+} phases are determined to have the weight ratio of Mg:Al:O = 4.73:17.63:77.65 and Eu:Mg:Al:O = 10.94:12.40:28.51:48.15, respectively. The EDAX data demonstrate that the atomic ratios of the elements are very close to their stoichiometric amounts [46]. The successful substitution of Eu^{3+} in $MgAl_2O_4$ crystals was also confirmed by EDAX analysis, as is shown in spectra (Fig. 9b). Figure 9(c) represents the histogram of $MgAl_2O_4$:xEu^{3+} samples in weight%. The possible peaks that are presented are associated to the above elements, while the extra peaks in the spectrum may be attributed to gold and carbon tape, which were added during coating for the EDAX spectroscopic analysis [43].

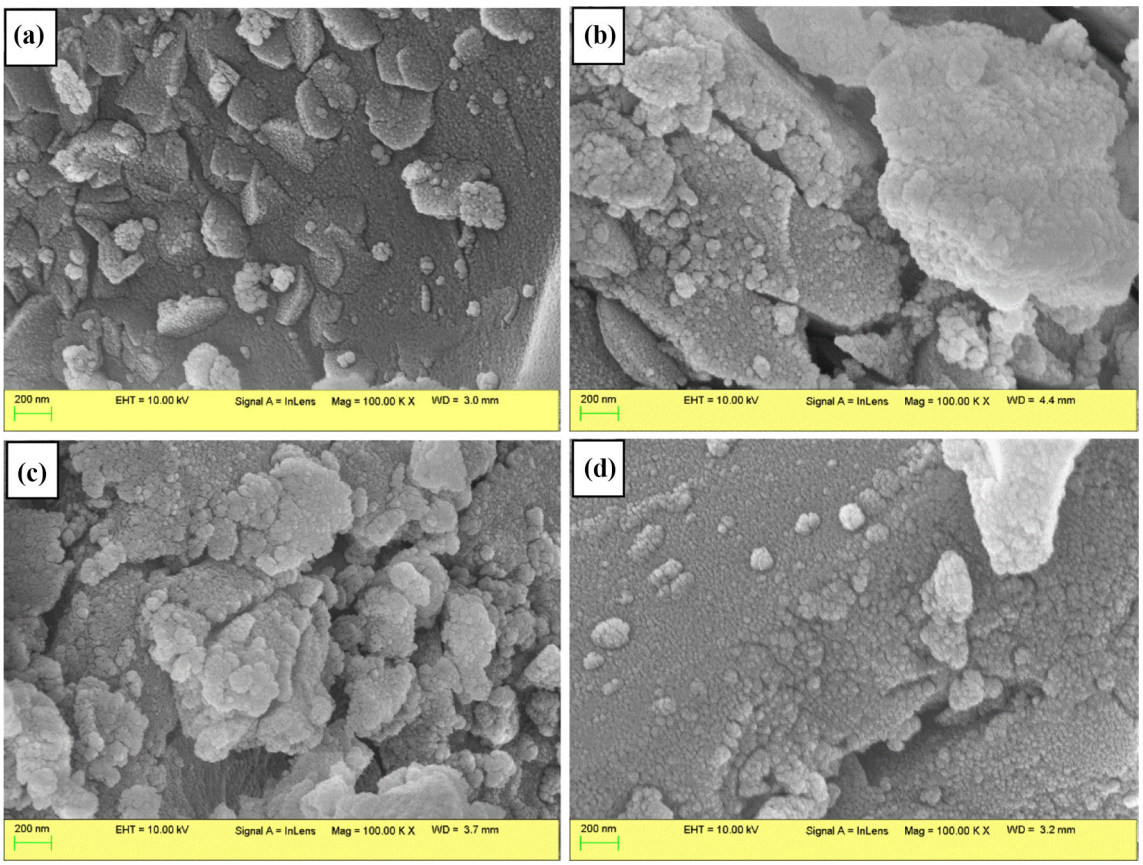

Fig. 7 FESEM images of prepared $MgAl_2O_4$:xEu^{3+} phosphors at different magnifications. **a** pure **b** $x = 0.02$ (c) $x = 0.06$ **d** $x = 0.10$

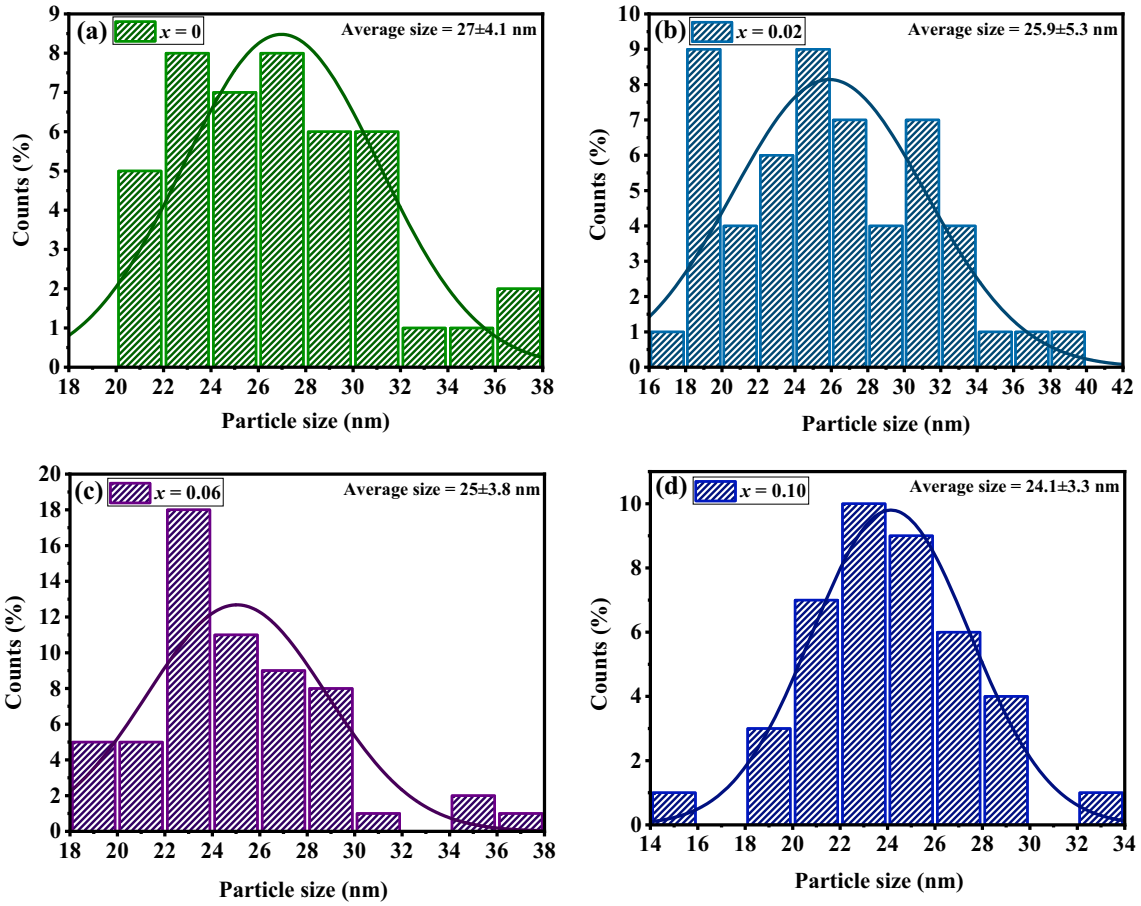

Fig. 8 Average particle size distribution histogram graph (FESEM) for pure and selected Eu^{3+}-doped $MgAl_2O_4$ samples

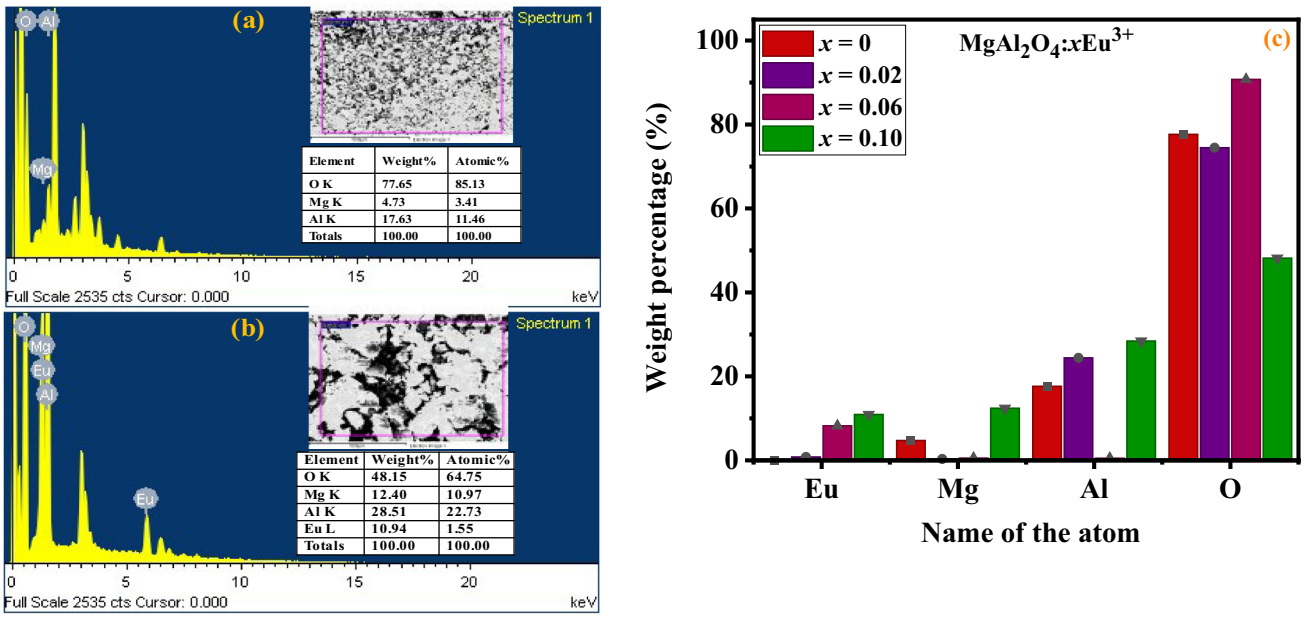

Fig. 9 Elemental analysis of $MgAl_2O_4$:xEu^{3+} phosphors **a** pure; and **b** $x = 0.10$; respectively. **c** is the corresponding histogram representation in weight%

3.7 HRTEM with SAED analysis

The microstructure of the host and 10% Eu^{3+}-doped $MgAl_2O_4$ nanopowder samples were examined by HRTEM as shown in Fig. 10. HRTEM images in Fig. 10a, d demonstrate that the particles within the as-synthesized samples are composed of several nanosized crystallites of spherical shape and the average crystallite size is found to be 12.1 ± 2.4 nm, and 11.4 ± 2.8 nm for host and 10% Eu^{3+}-doped $MgAl_2O_4$ NPs, respectively (Fig. 11), in agreement to the XRD crystallite sizes presented in Fig. 3(a) [27]. The obtained rings in selected area electron diffraction (SAED) pattern of host and 10% Eu^{3+}-doped samples are illustrated in Fig. 10c, f, and have been indexed perfectly to highly crystalline pure cubic phase of the spinel structure, which agrees well with the XRD results [47]. The interplanar distance between the adjacent planes was estimated to be 4.63

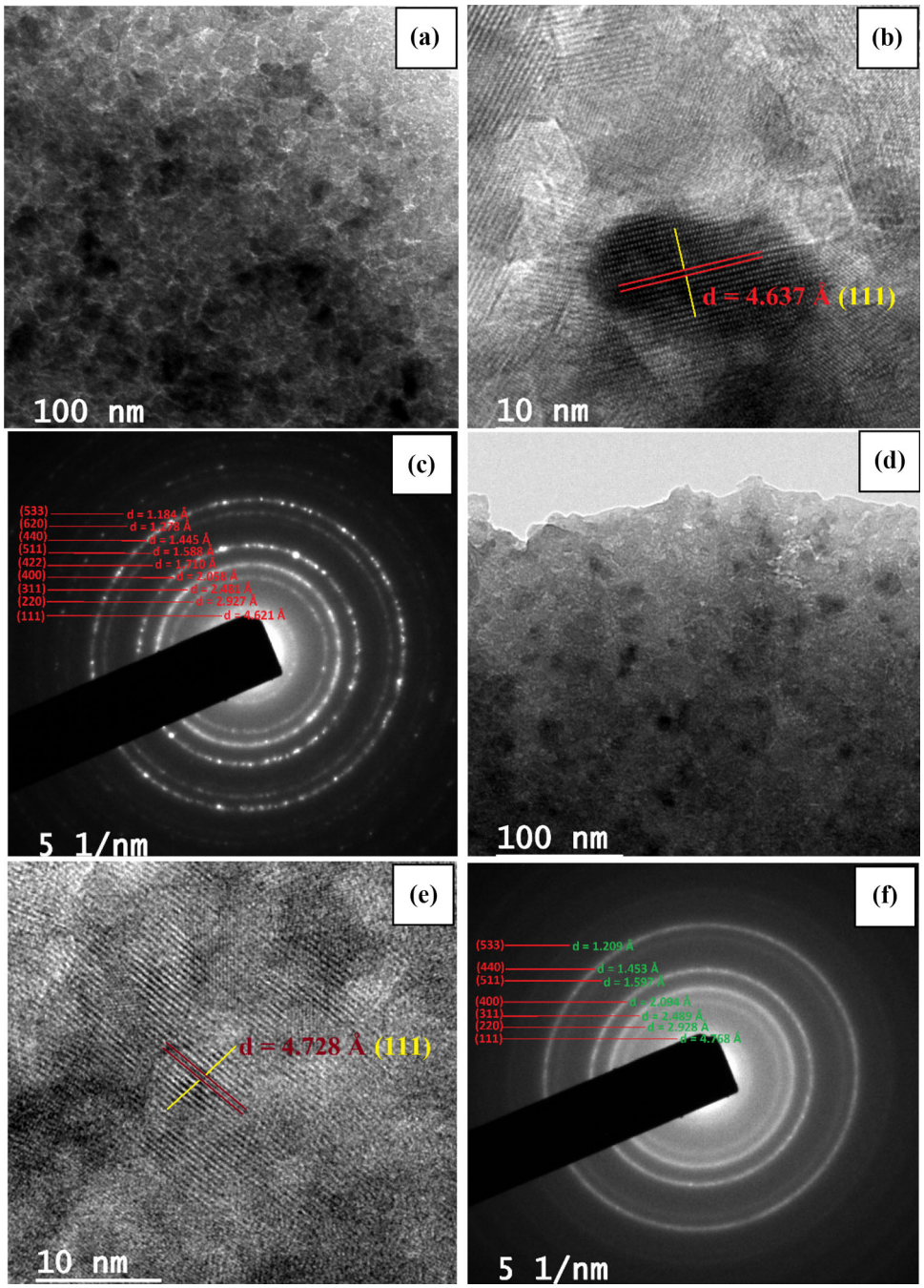

Fig. 10 TEM images of pure $MgAl_2O_4$ nanoparticles calcined at 950 °C for 12 h; **a** low-magnification TEM, **b** HRTEM, and **c** SAED spectrum and TEM images of $MgAl_2O_4$:10%Eu^{3+} nanoparticles calcined at 950 °C for 12 h; (**d**) low-magnification TEM, **e** HRTEM, and **f** SAED spectrum

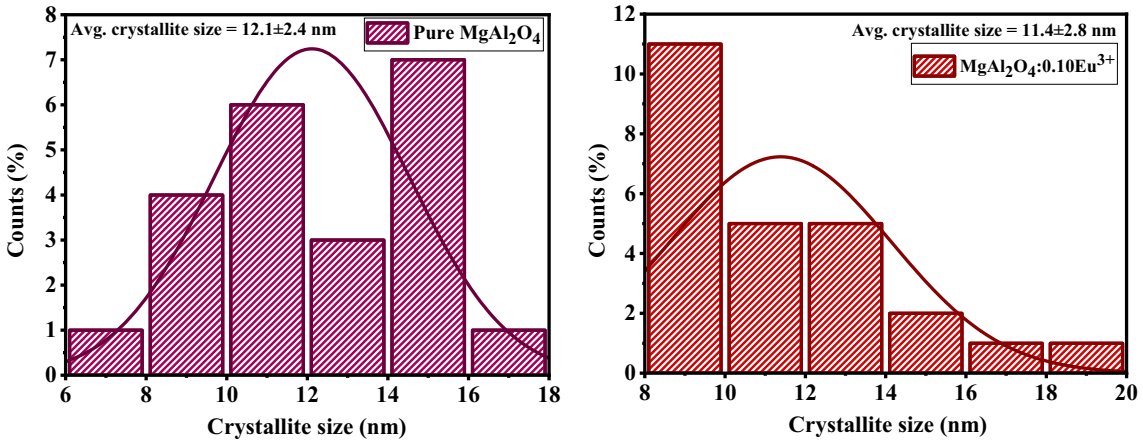

Fig. 11 Average crystallite size distribution histogram graph (HRTEM) for host and 10 mol% Eu^{3+}-doped $MgAl_2O_4$ samples

Å for undoped $MgAl_2O_4$ and 4.72 Å for $MgAl_2O_4$:10%Eu^{3+} from HRTEM images, which corresponds to (111) lattice plane (Fig. 10b, e).

3.8 Photoluminescence property studies

The photoluminescence emission spectrum of the $MgAl_2O_4$:xEu^{3+} nanophosphors annealed at 950 °C for 12 h, excited at 545 nm wavelength which exhibits four distinguishable peaks in the region of 580–740 nm is shown in Fig. 13a. These peaks are assigned to $^5D_0 \rightarrow {}^7F_J$ (J = 1, 2, 3, and 4) emission transitions, indicating the presence of Eu^{3+} ions in the $MgAl_2O_4$ host matrix and are named as $^5D_0 \rightarrow {}^7F_1$, $^5D_0 \rightarrow {}^7F_2$, $^5D_0 \rightarrow {}^7F_3$, and $^5D_0 \rightarrow {}^7F_4$ are observed around 590, 612, 654, and 703 nm, respectively [48]. From Fig. 13a, the hypersensitive $^5D_0 \rightarrow {}^7F_2$ (ΔJ = 2) transition peak centered around 612 nm is the most intense for all the samples of Eu^{3+} ion arising due to the shielding effect of 4f electrons by 5s and 5p electrons in the outermost shells of the europium ion [25]. It is obvious that the $^5D_0 \rightarrow {}^7F_1$ lines correspond to a magnetic dipole transition which will not change the crystal field strength around the Eu^{3+} ions and is independent of the symmetry. However, the $^5D_0 \rightarrow {}^7F_2$ lines that correspond to forced electric dipole transitions are hypersensitive and its emission intensity is highly dependent on site occupied by Eu^{3+} ions in the host lattice [49]. If the host matrix like $MgAl_2O_4$ is without inversion symmetry, the strong emission due to electrical dipole transition corresponding to 612 nm peak will appear and dominate in intensity when Eu^{3+} ions occupy noninversion symmetric Mg^{2+} sites of host lattice [50]. It is evident that the relative peak intensity of the emission spectra of Eu^{3+}-doped $MgAl_2O_4$ nanophosphor depends on the concentration of Eu^{3+} (Fig. 13a). The transition $^5D_0 \rightarrow {}^7F_2$ (612 nm) red emission intensity is much stronger than that of the $^5D_0 \rightarrow {}^7F_1$ (590 nm) orange emission. The energy level diagram of Eu^{3+} ion in $MgAl_2O_4$ is shown in Fig. 12.

In pure $MgAl_2O_4$, an energy band gap is created between the valence band (formed by O^{2-}) and the conduction band (formed by Mg^{2+} and Al^{3+}). The excitation process may take place in two ways, either by transferring the valence band electrons to the charge transfer band (CTB) or by jumping to the higher levels of Eu^{3+}. Under the excitation at 545 nm, the Eu^{3+} ions are excited from the ground state of $^7F_0$ to higher excited state [51]. After excitation, the excited Eu^{3+} ions (due to charge transfer) come to the $^5D_0$ state by nonradiative process. This process continues till $^5D_0$ energy level gets populated. Then the $^5D_0$ level is responsible for the fluorescence and it can make 4 transitions to the lower energy levels [27]. These four transitions correspond to four peaks in the PL emission spectra at 590 nm, 612 nm, 654 nm, and 703 nm. From Fig. 13(a), by increasing the Eu^{3+} content, the emission intensity of $^5D_0 \rightarrow {}^7F_2$ transition first reached to a maximum value at x = 0.04 from x = 0.02 and then decreased with an increase of Eu^{3+} concentration (x = 0.06, x = 0.08, and x = 0.10) due to a concentration quenching [25]. The phenomena of concentration quenching are ascribed due to energy transfer between (i) Eu^{3+} to Eu^{3+}, (ii) defect to Eu^{3+}, and (iii) Multiphonon-assisted electron–phonon

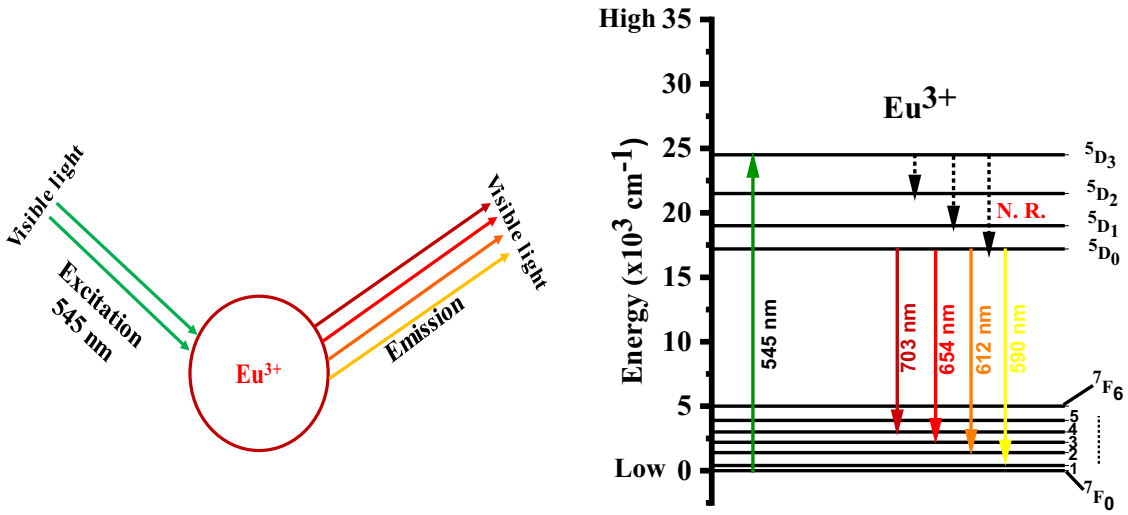

Fig. 12 Energy level diagram of Eu^{3+} ion in $MgAl_2O_4$:xEu^{3+} Phosphor

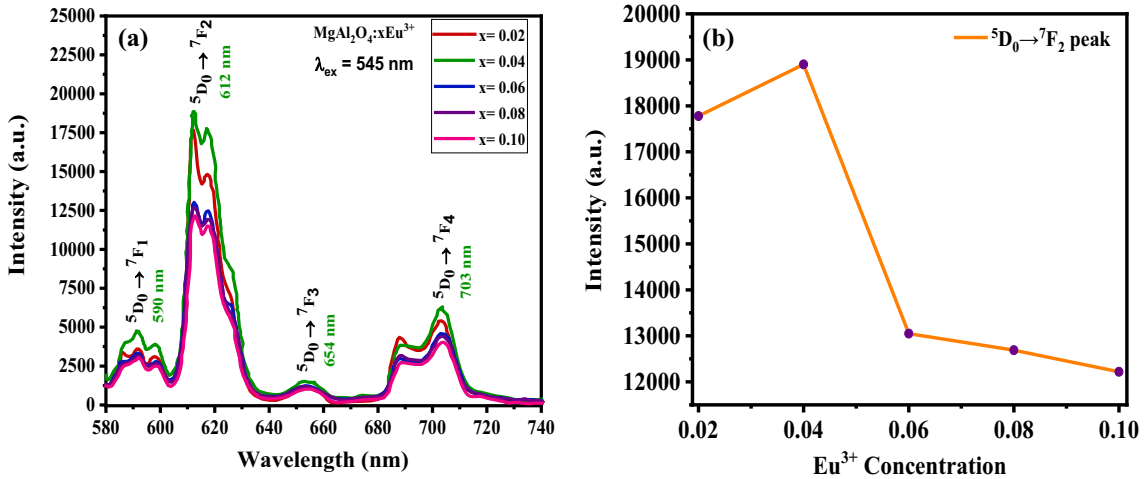

Fig. 13 **a** Room-temperature PL emission spectra of $MgAl_2O_4$:xEu^{3+} series; **b** PL emission intensity variation of $^5D_0 \rightarrow {}^7F_2$ in $MgAl_2O_4$:xEu^{3+} as a function of Eu^{3+} doping concentration

coupling. Hence, the dependence of luminescence intensity on the doping concentration of Eu^{3+} was studied and in $MgAl_2O_4$ the optimum content of Eu^{3+} was evaluated. This concentration dependence of emission intensity for the forced electric dipole transition of $^5D_0 - {}^7F_2$ at 612 nm is shown in Fig. 13(b). The type of energy transfer between the neighboring Eu^{3+} ions and the nature of quenching process can be identified by evaluating the relative or critical distance. According to Blasse's formula, the critical distance (R_c) can be expressed as

$$R_c = 2\left[\frac{3V}{(4\pi C_o N)}\right]^{(1/3)}, \quad (5)$$

where N is the number of host cations in the unit cell of the host matrix, C_o is the concentration of the activator Eu^{3+} ions, and V is the volume of the unit cell. For optimum concentration of C_o = 0.04, the measured R_c value between Eu^{3+} and Eu^{3+} is 10.2 Å, which is greater than the standard value of 5 Å for the rare-earth ions indicating that the type of interaction mechanism involved in the energy transfer is via a multipole–multipole interaction process and is the major cause of concentration quenching. Moreover, the variation of relative or critical distance between the Eu^{3+} ions in $MgAl_2O_4$:xEu^{3+} phosphor with the Eu^{3+} doping concentration is shown in Fig. 14. It can be observed that the relative distance

(R_c) is decreased gradually with increasing Eu^{3+} doping concentration [52].

The similar results of microstructure, morphology, and photoluminescence of $MgAl_2O_4$:Eu^{3+} red-emitting phosphors have been reported by C. Wenisch et al. [49]. Moreover, the PL emission results show that the Eu^{3+} ion was observed to be an isolated luminescence center and presented an intense red emission at 612 nm assigned to the $^5D_0 \rightarrow {}^7F_2$ transition with maximum intensity in $MgAl_2O_4$:$x$$Eu^{3+}$ phosphors. The optimum Eu^{3+} doping concentration was obtained to be 4% for the best luminescence process, eventually $MgAl_2O_4$:4%Eu^{3+} was chosen for the temperature-dependent PL emission study. Several researchers reported the optimum Eu^{3+} concentration in the range of 1 to 2 mol%. Also, the annealing process plays an important role in the successful substitution of Eu^{3+} ions into the $MgAl_2O_4$ host matrix and consequently influences its luminescent properties. So, the temperature-dependent PL analysis for $MgAl_2O_4$ with optimum doping concentration of Eu^{3+} were studied. The PL emission spectrum of 4% Eu^{3+}-doped $MgAl_2O_4$ sample annealed progressively at 650, 750, 850, and 950°C for 12 h recorded in the wavelength range from 580 to 740 nm excited at 545 nm is shown in Fig. 15a. It exhibits four $^5D_0 \rightarrow {}^7F_1$, $^5D_0 \rightarrow {}^7F_2$, $^5D_0 \rightarrow {}^7F_3$, and $^5D_0 \rightarrow {}^7F_4$ transitions arising from the Eu^{3+} ion with the $^5D_0 \rightarrow {}^7F_2$ dominant transition. From Fig. 15a of PL spectra, it is evident that the relative intensities of all the transitions were increased with increasing temperature for $MgAl_2O_4$:4%Eu^{3+} sample. This is due to the fact that the Eu^{3+} ions can be transferred more rapidly and successfully into the $MgAl_2O_4$ host lattice during thermal diffusion process as homogeneous purity phase. If the phosphor is thermally heated, the divalent europium ion oxidizes to Eu^{3+} state as the temperature increased and thereby creating more luminescent centers on the surface. Moreover, the energy transfer to the Eu^{3+} emission centers from the host turns into more significant as the material is treated at higher temperatures. The presence $^5D_0 \rightarrow {}^7F_2$ transition as more intense peak assigned to 612 nm of Eu^{3+} ions indicates that there will be no center of symmetry around Eu^{3+} ion in $MgAl_2O_4$ sample heated at 950°C when recorded under excitation at 545 nm [53]. Temperature dependence of the photoluminescence intensity of the forced electric dipole transition $^5D_0 - {}^7F_2$ of $MgAl_2O_4$:$x$$Eu^{3+}$ at optimum concentration (x = 4%Eu^{3+}) was analyzed and confirmed at excitation wavelength 545 nm (Fig. 15b).

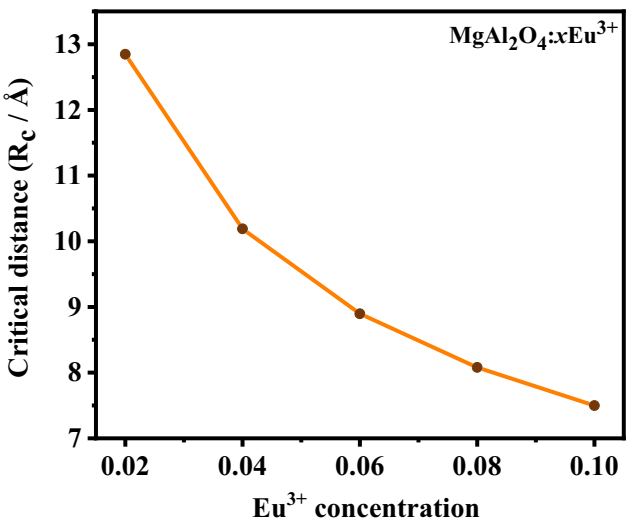

Fig. 14 The variation of critical distance with Eu^{3+} doping concentration of $MgAl_2O_4$:$x$$Eu^{3+}$ nanophosphor

3.9 CIE diagram

Figure 16 shows the Commission International de I'Eclairage (CIE) 1931 chromaticity diagram of $MgAl_2O_4$:$x$$Eu^{3+}$ nanophosphors calcined at 950 °C for 12 h. The perception of the color purity will be analyzed from the CIE chromaticity diagram with the help of emission color coordinates of the luminescent material. The CIE chromaticity color coordinates of the nanophosphors samples can be estimated by using three numbers (X, Y, Z) known as tristimulus colorimetry system from the emission spectra under the excitation at 545 nm wavelength [54]. The (x, y) color coordinates were evaluated based on emission spectra and found to lie in red region of CIE diagram (Fig. 16). Correlated color temperature (CCT) is another important parameter to assess the nanophosphor performance, which specifies the color appearance of light emitted was derived by CIE color coordinates [40, 55]. CCT is calculated by transforming the (x, y) coordinates of the light source to (u', v'). The CIE chromatic coordinates, CCT, (x, y) and color rendering index (CRI) of Eu^{3+}-doped $MgAl_2O_4$ samples are illustrated in Table 4.

On doping with Eu^{3+}, as there is no obvious change observed in the spectral profile of the CIE diagram, the color coordinates demonstrate that the

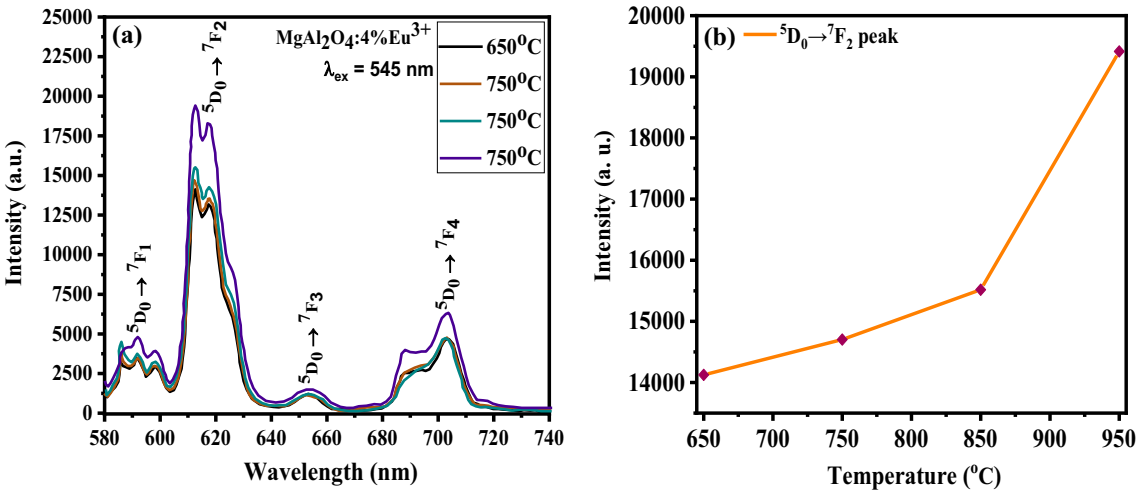

Fig. 15 **a** PL Emission spectra of $MgAl_2O_4$:4%Eu^{3+} phosphors; **b** PL emission intensity variation of $^5D_0 \rightarrow {}^7F_2$ in $MgAl_2O_4$:4%Eu^{3+} as a function of annealing temperature

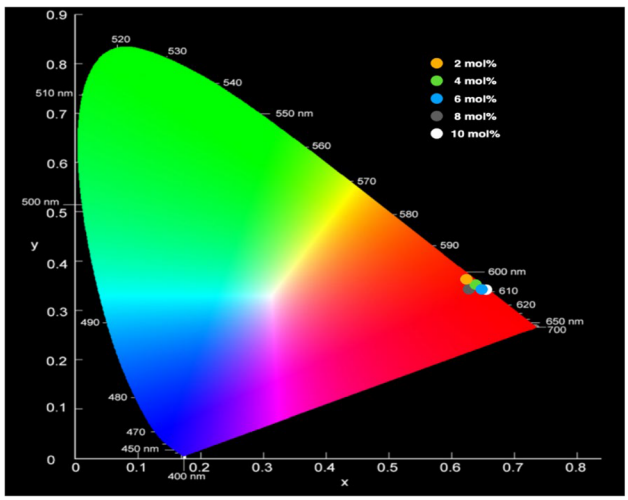

Fig. 16 CIE Chromaticity color coordinates diagram from emission spectra excited at 545 nm of $MgAl_2O_4$:xEu^{3+} nanophosphors calcined at 950 °C for 12 h

as-prepared $MgAl_2O_4$:xEu^{3+} nanophosphors emit intense bright red light (Fig. 16). The CIE diagram of 4% Eu^{3+}-doped $MgAl_2O_4$ at 950 °C presents CIE color coordinates of x = 0.6582 and y = 0.3415 showing the maximum intensity which are in good agreement with National Television System Committee (NTSC) red color coordinates (0.67, 0.33). This color tunability of the host lattice by changing the concentration of Eu^{3+} (2–10 mol%) is attributed to the possible energy transfer between the energy levels of activator (Eu^{3+}) ions. The calculated CCT values were found to be 2553.588–2618.01 K (< 5000 K), which is regarded as a cool red light. Thus, the observed high PL brightness along with excellent CCT value indicates that these phosphors can be highly useful in red LEDs for the production of artificial in red light and in solid-state display as well as other optical device applications [35, 56].

Table 4 CIE chromaticity color coordinates of Eu^{3+}-doped $MgAl_2O_4$ nanophosphors calcined at 950°C for 12 h

Sample	Concentration (mol %)	Color coordinates		u'	v'	CCT (K)	CRI
		x	y				
$MgAl_2O_4$:xEu^{3+}	2	0.6592	0.3405	0.4570	0.5313	2609.364	22
	4	0.6582	0.3415	0.4552	0.5316	2568.382	24
	6	0.6579	0.3419	0.4540	0.5316	2553.588	24
	8	0.6590	0.3401	0.4574	0.5311	2618.01	23
	10	0.6579	0.3411	0.4556	0.5314	2575.439	24

4 Conclusions

In summary, synthesis of undoped and Eu^{3+}-doped $MgAl_2O_4$ red-emitting nanophosphors with different Eu^{3+} doping concentrations have been achieved by the nitrate–citrate gel combustion route, which is a simple and cost-effective chemical process. The powder XRD pattern shows that Eu^{3+} is successfully doped in the host crystal lattice. The average crystallite size of nanophosphors decreased from 12.1 to 8.5 nm with increasing Eu^{3+} doping content. The TGA combined with DTG results showed that single-phase $MgAl_2O_4$:-$x Eu^{3+}$ spinel begins to form at around 600 °C. Vibration bands of the as-prepared samples corresponding to the presence of AlO_6 groups in FTIR spectra are related to the inorganic network. The band gap energy of the host and Eu^{3+}-doped phosphors was estimated from the UV–Vis spectra using Tauc's plot and is found to vary between 5.08 and 5.19 eV due to ionic exchange, indicating that E_g depends on Eu^{3+} content. The charge transfer $O^{2-} \rightarrow Al^{3+}$ transition as a result of the excitation of electrons into the conduction band of $MgAl_2O_4$ largely influence the absorption band at 250 nm. The FESEM studies showed the relatively spherical morphology of the agglomerated nanoparticles with average particle size ~ 30 nm and successful substitution of Eu^{3+} in $MgAl_2O_4$ host lattice, which was also confirmed by EDAX analysis. The HRTEM images demonstrated that the obtained $MgAl_2O_4$:$x Eu^{3+}$ powders are in nanometer dimensions with average crystallite size 11.4 ± 2.8–12.1 ± 2.4 nm. The hypersensitive $^5D_0 \rightarrow {}^7F_2$ (ΔJ = 2) transition at 612 nm is attributed to the well-known red emission Eu^{3+} electric dipole transition (EDT) and is most intense. The process of quantum quenching is observed in $MgAl_2O_4$:$x Eu^{3+}$ and the optimum value of doping concentration is obtained to be 4 mol% Eu^{3+} from the emission spectra. Moreover, the improved photoluminescence intensity of $MgAl_2O_4$:4%Eu^{3+} sample at progressively high temperatures has also been characterized. The as-prepared $MgAl_2O_4$:$x Eu^{3+}$ phosphor material shows bright red emission along with good CCT values, which make it useful as an important phosphor for red emission LED applications.

Acknowledgements

The authors express their sincere thanks to the DST-FIST Central Instrumentation Laboratory, Government College Autonomous, Rajahmundry, Andhra Pradesh and SSCU, IISc, Bengaluru for providing lab and instrumentation facilities for the preparation of Luminescent Nanomaterials.

Authors contribution

RRK: Conceptualization, Methodology, and Supervision; BNR, EBS, and DSLP: Experimentation and Writing—Original draft preparation; PTR: Visualization and data Investigation; KS: Writing—Reviewing and Editing.

Data availability

The authors are ready to provide any research data, which have been mentioned in the manuscript on request.

Declarations

Conflict of interest There are no conflicts of interest.

References

1. R.C. Ropp, *Luminescence and the Solid State*, 2nd edn. (Elsevier, Amsterdam, 2004)
2. D. Levy, A. Pavese, M. Hanfland, Am. Mineral 88, 93 (2003)
3. B.P. Uberuaga, D. Bacorisen, R. Smith, J.A. Ball, R.W. Grimes, A.F. Voter, K.E. Sickafus, Phys. Rev. B 75, 104116 (2007)
4. S.K. Mohan, R. Sarkar, Mater. Design 110, 145 (2016)
5. F.Y. Cui, A. Kundu, A. Krause, M.P. Harmer, R.P. Vinci, Acta Mater 148, 320 (2018)
6. N. Habibi, Y. Wang, H. Arandiyan, M. Rezaei, Adv. Powder Technol. 28, 1249 (2017)
7. R. Nakhowong, S. Kiennork, P. Wongwanwattana, T. Seetawan, R. Chueachot, Mater. Lett. 220, 234 (2018)
8. S. Sinhamahapatra, M. Shamim, H.S. Tripathi, A. Ghosh, K. Dana, Ceram. Int. 42, 9204 (2016)
9. O. Shpotyuk, A. Ingram, H. Klym, M. Vakiv, I. Hadzaman, J. Filipecki, J. Eur. Ceram. Soc. 25, 2981 (2005)
10. J. Jeon, Y. Kang, J.H. Park, Y. Chung, Ceram. Int. 43, 15074 (2017)
11. F. Li, Y. Zhao, Y. Liu, Y. Hao, R. Liu, D. Zhao, Chem. Eng. J. 173, 750 (2011)
12. G. Gusmano, G. Montesperelli, E. Traversa, G. Mattogno, J Am. Ceramic Soc. 76, 743 (1993)

13. C. Dlamini, M.R. Mhlongo, L.F. Koao, T.E. Motaung, T.T. Hlatshwayo, S.V. Motloung, Appl. Phys. A 126, 75 (2020)
14. T. Sato, M. Shirai, K. Tanaka, Y. Kawabe, E. Hanamura, J. Lumin 114, 155 (2005)
15. P.J. Dereń, K. Maleszka-Bagińska, P. Głuchowski, M.A. Małecka, J. Alloys Compd. 525, 39 (2012)
16. I. Omkaram, S. Buddhudu, Opt. Mater. 32, 8 (2009)
17. Q. Sai, C. Xia, H. Rao, X. Xu, G. Zhou, P. Xu, J. Lumin. 131, 2359 (2011)
18. V. Singh, V. Kumar Rai, S. Watanabe, T.K. Gundu Rao, L. Badie, I. Ledoux-Rak, Y.-D. Jho, Appl. Phys. B 108, 437 (2012)
19. A. Jouini, H. Sato, A. Yoshikawa, T. Fukuda, G. Boulon, K. Kato, E. Hanamura, J. Cryst. Growth 287, 313 (2006)
20. V. Singh, G. Sivaramaiah, J.L. Rao, S.H. Kim, J. Lumin. 143, 162 (2013)
21. J. Qiao, Z. Xia, J. Appl. Phys. 129, 200903 (2021)
22. I. Omkaram, G. Seeta Rama, Raju, S. Buddhudu, J. Phys. Chem. Solids 69, 2066 (2008)
23. A.S. Maia, R. Stefani, C.A. Kodaira, M.C.F.C. Felinto, E.E.S. Teotonio, H.F. Brito, Opt. Mater. 31, 440 (2008)
24. W. Nantharak, W. Wattanathana, W. Klysubun, T. Rimpongpisarn, C. Veranitisagul, N. Koonsaeng, A. Laobuthee, J. Alloys Compd. 701, 1019 (2017)
25. I. Omkaram, B. Vengala Rao, S. Buddhudu, J. Alloys Compd. 474, 565 (2009)
26. R. Djenadic, M. Botros, H. Hahn, Solid State Ionics 287, 71 (2016)
27. V. Maphiri, B. Dejene, T. Motaung, T. Hlatshwayo, O. Ndwandwe, S. Motloung, Nanomater Nanotechnol 8, 184798041880064 (2018)
28. T. Yamanaka, Y. Takéuchi, Z. Für Kristallographie - Crystalline Mater. 165, 65 (1983)
29. U.D. Wdowik, K. Parliński, A. Siegel, J. Phys. Chem. Solids 67, 1477 (2006)
30. G.B. Andreozzi, F. Princivalle, H. Skogby, A. Della Giusta, Am. Min. 85, 1164 (2000)
31. S. Sanjabi, A. Obeydavi, J. Alloys Compd. 645, 535 (2015)
32. S.K. Behera, P. Barpanda, S.K. Pratihar, S. Bhattacharyya, Mater. Lett. 58, 1451 (2004)
33. S. Tripathy, D.S. Saini, D. Bhattacharya, J. Asian. Ceam. Soc. 4, 149 (2016)
34. M.F. Zawrah, H. Hamaad, S. Meky, Ceram. Int. 33, 969 (2007)
35. C. Pratapkumar, S.C. Prashantha, H. Nagabhushana, D.M. Jnaneshwara, J. Science: Adv. Mater. Devices 3, 464 (2018)
36. C. Luan, D. Yuan, X. Duan, H. Sun, G. Zhang, S. Guo, Z. Sun, D. Pan, X. Shi, Z. Li, J. Sol-Gel Sci. Technol. 38, 245 (2006)
37. A.K. Adak, S.K. Saha, P. Pramanik, J. Mater. Sci. Lett. 16, 234 (1997)
38. Y.-J. Lin, C.-J. Wu, Surf. Coat. Technol. 88, 239 (1997)
39. S.V. Motloung, B.F. Dejene, R.E. Kroon, O.M. Ntwaeaborwa, H.C. Swart, T.E. Motaung, Optik 131, 705 (2017)
40. P. Du, J.S. Yu, Sci. Rep. 7, 11953 (2017)
41. A. Ali, I.H. Gul, M.Z. Khan, F. Javaid, J. Korean Ceram. Soc. (2022)
42. M. Dongol, M.M. El-Nahass, A. El-Denglawey, A.F. Elhady, A.A. Abuelwafa, Curr. Appl. Phys. 12, 1178 (2012)
43. A. Mazhar, A.H. Khoja, A.K. Azad, F. Mushtaq, S.R. Naqvi, S. Shakir, M. Hassan, R. Liaquat, M. Anwar, Energies 14, 3347 (2021)
44. P. Pathak, R. Kurchania, Phys. B: Condens. Matter. 545, 119 (2018)
45. S. Gul, M.A. Yousuf, A. Anwar, M.F. Warsi, P.O. Agboola, I. Shakir, M. Shahid, Ceram. Int. 46, 14195 (2020)
46. B.V. Naveen Kumar, K. Venkata Rao, E. Basha Shaik, Y. Nirmal Rajeev, K. Ramachandra Rao, S. Cole, Luminescence 37, 1942 (2022)
47. M.G. Brik, J. Papan, D.J. Jovanović, M.D. Dramićanin, J. Lumin. 177, 145 (2016)
48. I.V. Beketov, A.I. Medvedev, O.M. Samatov, A.V. Spirina, K.I. Shabanova, J. Alloys Compd. 586, S472 (2014)
49. C. Wenisch, H.-D. Kurland, J. Grabow, F.A. Müller, J. Am. Ceram. Soc. 99, 2561 (2016)
50. S. Saha, S. Das, U.K. Ghorai, N. Mazumder, B.K. Gupta, K.K. Chattopadhyay, Dalton Trans. 42, 12965 (2013)
51. J. Wu, J. Wang, J. Lin, Y. Xiao, G. Yue, M. Huang, Z. Lan, Y. Huang, L. Fan, S. Yin, T. Sato, Sci. Rep. 3, 2058 (2013)
52. W. Ran, H.M. Noh, S.H. Park, B.K. Moon, J.H. Jeong, J.H. Kim, J. Shi, Sci. Rep. 8, 5936 (2018)
53. S.V. Motloung, B.F. Dejene, O.M. Ntwaeaborwa, H.C. Swart, R.E. Kroon, Chem. Phys. 487, 75 (2017)
54. T. Samuel, Ch.S. Kamal, K. Sujatha, V. Veeraiah, Y. Ramakrishana, K.R. Rao, Optik 127, 10575 (2016)
55. C. Pratapkumar, S.C. Prashantha, H. Nagabhushana, M.R. Anilkumar, C.R. Ravikumar, H.P. Nagaswarupa, D.M. Jnaneshwara, J. Alloys Compd. 728, 1124 (2017)
56. E.B. Shaik, B.V.N. Kumar, S.K. Chirauri, K.R. Rao, J. Mater. Sci: Mater. Electron. 33, 105 (2022)